Ultrasonics 149 (2025) 107571

Contents lists available at ScienceDirect

Ultrasonics

journal homepage: www.elsevier.com/locate/ultras

Sensitivity of Lamb waves in viscoelastic polymer plates to surface contamination

Jakub Spytek [a,b,*], Daniel A. Kiefer [a], Ros Kiri Ing [a], Claire Prada [a], Jérôme Grando [c], Julien de Rosny [a]

[a] Institut Langevin, ESPCI Paris, Université PSL, CNRS, 1 rue Jussieu, Paris, 75005, France
[b] AGH University of Krakow, Department of Mechanics and Robotics, al. A. Mickiewicza 30, Krakow, 30-059, Poland
[c] Plastic Omnium, Avenue du Bois des Vergnes, Sainte-Julie, 01150, France

ARTICLE INFO

Keywords:
Lamb waves
Viscoelastic material
Thermoformed polymer
SHM
Surface contamination
Local wavenumber estimation

ABSTRACT

Detecting surface contamination on thin thermoformed polymer plates is a critical issue for various industrial applications. Lamb waves offer a promising solution, though their effectiveness is challenged by the strong attenuation and anisotropy of the polymer plates. This issue is addressed in the context of a calcium carbonate ($CaCO_3$) layer deposited on a polypropylene (PP) plate. First, the viscoelastic properties of the PP material are determined using a genetic algorithm inversion of data measured with a scanning laser vibrometer. Second, using a bi-layer plate model, the elastic properties and thickness of the $CaCO_3$ layer are estimated. Based on the model, the sensitivity analysis is performed, demonstrating considerable effectiveness of the A1 Lamb mode in detecting thin layers of $CaCO_3$ compared to Lamb modes A0 and S0. Finally, a direct application of this work is illustrated through in-situ monitoring of $CaCO_3$ contaminants using a straightforward inter-transducer measurement.

1. Introduction

Modern automotive industry employs advanced sensors for Simultaneous Localization and Mapping (SLAM) of the vehicle's surroundings [1]. The most sophisticated sensors, based on radio detection and ranging (RADAR) or light detection and ranging (LIDAR) systems, are often installed behind the plate-like components of the vehicle for additional protection and aesthetic reasons. However, the presence of contaminations on the surface of these components may block the signal of SLAM sensors. Therefore, there is a need for a monitoring system that is capable of detecting and localizing contaminants such as dirt, ice or water droplets to provide a feedback to the SLAM. In this work, we explore a new modality to detect the surface contaminants using ultrasonic guided waves, specifically Lamb waves, which can be transmitted through the area of interest without obscuring the signal used for SLAM.

The Lamb waves have been widely used for the monitoring in different types of structures, including metal plates [2], composites [3] or adhesively bonded joints [4]. A typical use of Lamb waves is based on a network of transducers embedded in the structure in order to detect defects. More advanced methods involve localization and characterization of defects, e.g. using tomography [5–7] or phased arrays [8]. In the majority of applications, the Lamb waves were employed to detect different types of structural defects such as cracks, delaminations or corrosion. In some cases the Lamb waves were used to detect ice on the plates' surface, e.g. using principal component analysis [9] or probability-based reconstruction algorithm (PRA) [10]. However, the sensitivity of Lamb waves to other types of contamination, such as dirt or mud, has not yet been explored in the state of the art. Moreover, the information on the use of Lamb waves in thermoformed plate-like structures is also limited. Due to the widespread use of such components, there is a need for a more detailed analysis of Lamb waves' behavior in thermoformed polymer plates.

To achieve the most effective detection of surface contaminants in thermoformed polymer plates using Lamb waves, the material properties of both the substrate and the contaminant layer must be determined beforehand. The estimation of material properties can be realized using different approaches including static tests, vibrational methods or wave propagation methods [11]. The wave-based methods may be realized using bulk waves [12] or Lamb waves [13]. The characterization of thin structures with bulk waves has its limitations [13], such as relatively narrow excitation frequency bandwidth, estimation errors due to reflections at plate boundaries and the need for prior knowledge of the material symmetry axis. The methods based on Lamb waves overcome these limitations, but require much more sophisticated

* Corresponding author at: AGH University of Krakow, Department of Mechanics and Robotics, al. A. Mickiewicza 30, Krakow, 30-059, Poland.
E-mail address: jspytek@agh.edu.pl (J. Spytek).

https://doi.org/10.1016/j.ultras.2025.107571
Received 20 November 2023; Received in revised form 1 October 2024; Accepted 9 January 2025
Available online 15 January 2025
0041-624X/

inversion procedure. In general, parameter estimation using Lamb waves is performed on measurements acquired in multiple spatial points, although under some specific measurement conditions only two points can be sufficient [14]. For an inversion procedure, an objective function is often built from space–time data using frequency–wavenumber pairs corresponding to the experimental dispersion curves [15]. Several different inversion procedures have been used with Lamb waves, including particle swarm optimization [13,15–17], genetic algorithm [18–21], simulated annealing [22], gradient descent [23], bound-constrained optimization [24], deep learning [14] or machine learning [25]. Deep and machine learning techniques are more suited towards real-time applications, as the trained neural network can provide accurate estimates of elastic parameters in seconds, while other inversion methods often need hours for computing numerous iterations. On the other hand, a lot of data is required to train neural networks, so numerical simulations are often used to obtain the training data. The inversion methods based on Lamb waves have been used to estimate elastic [13,15,16,19,20,22,26] as well as viscoelastic [17,24] parameters of the material. However, the problem of identifying a full viscoelastic orthotropic model with 18 independent parameters can be very challenging [17]. Such a problem requires space–time data with broad frequency response and well-resolved modes. For this purpose, postprocessing algorithms are often used to better extract the complex wavenumbers of the modes from frequency–wavenumber data [17].

To estimate the properties of the contamination, the wavenumbers need to be extracted from the space–time Lamb wave measurements corresponding only to the area of contamination. To this end, the techniques of full-field processing known as Acoustic Wavenumber Spectroscopy (AWS) or Local Wavenumber Estimation (LWE) were used previously [27,28]. These techniques enable estimating local wavenumber values at specific frequencies, which can be used for detection and characterization of damage. These techniques usually work for a single mode, therefore a mode filtration is often used in frequency–wavenumber domain. The local mapping of wavenumber values is usually performed by using windowing functions in spatial (AWS) or wavenumber (LWE) domains. These techniques have been successfully used for imaging of thickness changes [27,29], corrosion [30] as well as delaminations in Carbon Fiber-Reinforced Polymers (CFRP) [31,32] and metal multi-layer plates [33]. The use of windowing functions in LWE or AWS requires careful consideration. For material characterization, depending on the window length, a compromise must be found between localization accuracy and wavenumber estimation. To partially avoid this issue, we propose to use a technique similar to LWE and AWS, which is based on calculating the Laplacian of the space–time wavefield in each position. Thanks to this approach, there is no need for applying a windowing function for the estimation of the local wavenumber. Moreover, this approach can also be used to estimate the local attenuation coefficient, which is vital for the estimation of viscoelastic properties.

In this work, we investigate the influence of surface contaminants on the Lamb waves propagating in thermoformed polymer plates for the purpose of detection. To this end, we first estimate viscoeleastic properties of polypropylene plates using a genetic algorithm for the parametric inversion problem. Secondly, we perform a full-field imaging of the plate with surface contamination added in the form of a $CaCO_3$ layer, which is meant to simulate a dirt layer deposited on the surface of the plate. For these data sets, we estimate frequency-dependent local wavenumber values from the area of the deposited contaminant. Based on the local wavenumber values for different amounts of deposited contamination, we determine the material properties of the $CaCO_3$ layer using an inversion procedure with a bi-layer plate model. Using the properties of both the polypropylene and the $CaCO_3$ we perform a sensitivity analysis to determine the most suitable Lamb modes and frequency range for the detection of contamination. Finally, we present an example of a simple inter-transducer measurement to prove the validity of Lamb wave based monitoring system.

2. Material characterization procedure

In this work, we assess the detectability of surface contamination on a thin-walled polypropylene sample with guided waves propagating in the layered medium. Specifically, we use a standard bi-layer plate model [34,35]. The wavefield in both layers is governed by the equations of linear elasticity. We assume a layer of $CaCO_3$ contaminant that is rigidly connected to the layer of polypropylene, meaning continuity of displacements and tractions is imposed at the interface. The top and bottom surfaces are traction-free. Each layer is defined by a thickness, elastic constants and mass density. We then calculate the dispersion curves of guided waves using a semi-analytical procedure implemented in the publicly available software `GEWtool` [36,37]. The computation consists in discretizing the boundary-value problem that describes guided wave propagation using Spectral Elements, i.e., high-order Finite Elements [38,39], and subsequently obtaining the dispersion relation by solving the resulting standard eigenvalue problem.

To detect a contaminant, the material properties of both the substrate and the contaminant layer must be determined first. The characterization of the polypropylene sample and the surface contamination requires several signal processing techniques, which are described in this section. Firstly, Section 2.1 describes the inversion procedure for the global estimation of elastic parameters based on the full-field measurements of Lamb waves. Secondly, Section 2.2 demonstrates the Laplacian method, which is used for the estimation of the local wavenumber and attenuation of Lamb waves for different frequencies. The frequency-dependent attenuation is then used together with the globally estimated elastic parameters to obtain viscous coefficients by fitting the imaginary part of theoretical dispersion curves to the attenuation curves. As a result, viscoelastic properties of the plate are obtained. In the next step, the Laplacian method is used to estimate the local wavenumber corresponding to the area with the layer of contaminant. For this purpose, the inversion procedure (Section 2.1) is applied to estimate the properties of $CaCO_3$ by fitting theoretical dispersion curves from a bi-layer plate model to the estimated local wavenumber values.

2.1. Inversion procedure for elastic parameter estimation

The inversion procedure used in this work is based on the space–time measurements of the propagating Lamb waves. The normal surface displacement $u(x,t)$ is measured over time t and multiple locations x using a full-field scanning technique. The multidimensional Fourier transform of $u(x,t)$ provides the experimental dispersion curves $U(k,\omega)$. In order to estimate material parameters based on $U(k,\omega)$, we use an inversion procedure coupled with a genetic algorithm implementation based on the work by Bochud et al. [19]. The approach is described in Fig. 1. Each population member contains a set of direction-dependent material parameters: Young's Modulus E_i, Poisson's ratio ν_{ij}, shear modulus G_{ij} and density ρ. The elastic parameters E_i, ν_{ij} and G_{ij} can also be represented in the form of a stiffness matrix C_{ij}, e.g., using Voigt notation. The relationship between the engineering constants and the coefficients of the matrix C_{ij} can be found in Appendix, based on [40]. Assuming a known thickness of the plate h, a set of theoretical dispersion curves $k_m(\omega)$ is calculated, where m is the number of a Lamb mode. The calculated dispersion curves are then mapped onto a 2D mask $M(k,\omega)$, where for each frequency–wavenumber pair $k_m(\omega)$ the mask value is set to 1. The cost function (F) to be maximized using the genetic algorithm can be therefore defined as:

$$F = \sum_{k,\omega} M(k,\omega) \cdot U(k,\omega) \tag{1}$$

The value of F is maximized if the theoretical dispersion curves overlap with the experimental dispersion curves. The sensitivity of this approach depends on the modal distribution of energy in frequency–wavenumber space $U(k,\omega)$. Therefore, higher-order modes which are

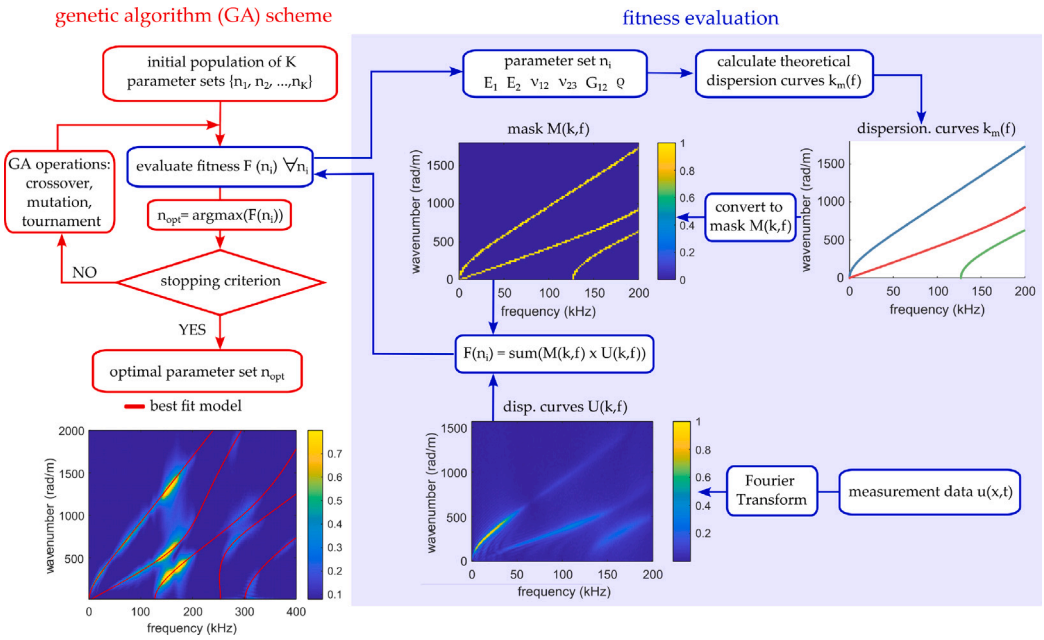

Fig. 1. The scheme of the inversion procedure to estimate material parameters from experimental dispersion curves.

subject to higher attenuation may be underrepresented in the curve-fitting process. We can account for that in two ways. Firstly, applying mode- and frequency-dependent weights on the mask window $M(k,\omega)$, e.g. by increasing the gain for higher-frequency modes. Secondly, by scaling the amplitudes of the individual mode in the $U(k,\omega)$ data set, to make the amplitude distribution more uniform. Practically, this approach can be realized by the manual filtration of particular modes in the (k,ω) space and normalizing their amplitudes, while being cautious not the amplify the noise contribution too much. The band-pass mode filter can be realized based on a Gaussian window, given by the following formula:

$$W(k,\omega) = \exp\left(-\frac{(|k| - k_c(\omega))^2}{2B_m^2}\right) \tag{2}$$

where $k_c(\omega)$ is a set of center wavenumbers of the filter, typically following a particular Lamb mode, and B_m indicates the width of the filter.

2.2. Wavenumber and attenuation estimation using Laplacian

The Laplacian algorithm proposed in this work is a signal processing technique that can be used to obtain local estimates of both the wavenumber and the attenuation of Lamb modes. To demonstrate the theoretical principles behind this method, let us assume an equation for a wave $u(x,\omega)$ propagating in the direction x in frequency domain ω:

$$u(x,\omega) = A(\omega)e^{-ik_M x} \tag{3}$$

where k_M is the sum of the real wavenumber k_R and $i\alpha$, where α is the attenuation coefficient. Calculating the Laplacian of the displacement field $\Delta u(x,\omega)$ and neglecting the second order term in α yields:

$$\Delta u(x,\omega) = -k_M^2 u(x,\omega) = -(k_R + i\alpha)^2 u(x,\omega) \approx \left(-k_R^2 + i\frac{2\omega\alpha}{c}\right)u(x,\omega) \tag{4}$$

with $k_R = \frac{\omega}{c}$, where c is the phase velocity. This relationship can then be used to estimate a local wavenumber $k_R(x,\omega)$ and attenuation $\alpha(x,\omega)$ directly from the Laplacian of the measured wavefield $\Delta u(x,\omega)$ for any frequency ω using the following equations:

$$R(x,\omega) = \frac{\Delta u(x,\omega)}{u(x,\omega)} = -k_R^2(x,\omega) + i\frac{2\omega}{c}\alpha(x,\omega) \tag{5}$$

$$k_R(x,\omega) = \sqrt{-\mathbb{R}(R(\omega))} \tag{6}$$

$$\alpha(x,\omega) = \frac{\mathbb{I}(R(x,\omega))c}{2\omega} \tag{7}$$

where $\mathbb{R}$ and $\mathbb{I}$ stand for real and imaginary part, respectively. This approach works assuming a single mode is present in the wavefield $u(x,\omega)$. In practice, the Lamb wavefield is composed of several modes. Therefore prior to applying Eqs. (4)–(7), a mode filter given by Eq. (2) needs to be applied in frequency–wavenumber domain $U(k,\omega)$ to isolate a single mode information. The use of the mode filter has an additional benefit of reducing noise, which may greatly affect the local estimation due to the numerical calculation of the Laplacian.

The Laplacian method has two applications in the identification of material properties employed in this work. Firstly, the frequency-dependent attenuation curves are used for the estimation of viscoelastic material parameters. By fitting the imaginary part of the theoretical dispersion curves to the experimental attenuation curves, the viscous parameters of the material can be estimated. The viscous parameters are included in the material model obtained from the inversion procedure (Section 2.1) by adding the imaginary part to the elastic parameters of the stiffness matrix C, resulting in a complex stiffness matrix $C_c = C + iC'$. Using C_c in the calculation of theoretical dispersion curves results in complex wavenumbers, where the imaginary part is the attenuation of the Lamb modes. Therefore, the coefficients of the C' matrix are treated as parameters to obtain a fit to the attenuation plots.

Second, application of the Laplacian concerns the possibility to obtain local wavenumber values to estimate material properties corresponding to the contamination layer. These frequency–wavenumber values can once again be used in the inverse problem by fitting the theoretical dispersion curves from a bi-layer plate model, consisting of polypropylene and $CaCO_3$ layers. Assuming that the properties of the polypropylene are known from the previous analysis, the properties of $CaCO_3$ can be treated as unknowns in the inverse procedure. In the end, knowing the material properties of both the polypropylene as well as the $CaCO_3$ layer allows for more advanced theoretical analysis of the Lamb waves' sensitivity to surface contaminants.

3. Description of the experiment

The sample used in the experiments is a polypropylene plate provided by the company *Plastic Omnium*. The sample is rectangular

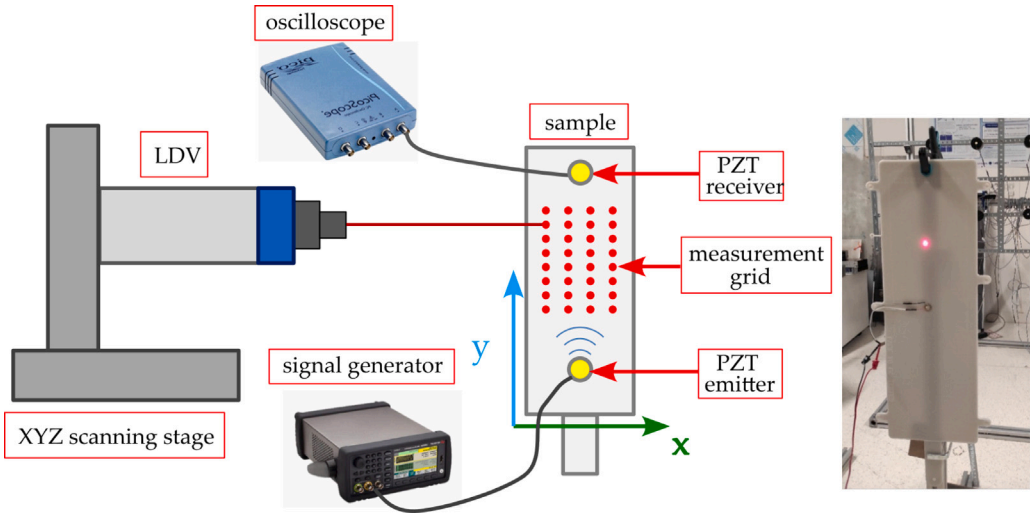

Fig. 2. Measurement setup for the parameter estimation. The Lamb waves are generated using a PZT transducer glued to the plate using epoxy adhesive and driven using the arbitrary waveform generator. The responses from the surface of the plate are measured with a Laser Doppler Vibrometer (LDV) mounted on the XYZ scanning stage.

with approximate dimensions of 196 × 591 × 3.4 mm, disregarding mounting elements. While the thickness of the plate varies by around ±0.1 mm in the inspected area, for the purpose of the further analysis it is assumed constant. The experimental equipment used in this work is presented in Fig. 2. For full-field signal acquisition, the *Polytec OFV-5000* Laser Doppler Vibrometer mounted on the XYZ scanning stage is used. To simplify the measurement, the vibrometer laser beam is oriented orthogonally to the surface of the plate, and the coordinates of the scanning points are taken from the encoder of the XYZ stage. The Lamb waves are excited using a PZT transducer glued to the plate using epoxy adhesive and driven using the arbitrary waveform generator *Agilent 33220A*. Additionally, inter-transducer measurements are acquired by a second PZT transducer located on the other side of the scanned area. The signals measured using LDV, PZT receiver, as well as the excitation signal are recorded using a *PicoScope 4000* series oscilloscope. The examined sample is mounted vertically to a fixed post using two clamps pressing on the top and bottom edges of the plate.

For the initial parameter estimation, a full-field scan is performed on the area of 99 × 159 mm with a spatial sampling of 1.5 mm, resulting in a mesh of 67 × 107 measurement points. The excitation signal is a frequency sweep in the range between 1 and 400 kHz, with an amplitude of 10 Vpp and a duration of 400 ms. The measured signals are sampled at 1 MHz frequency, and pulse compressed to increase the signal-to-noise ratio (SNR) [41]. The resulting data set is denoted as **DataA**.

The surface contamination is applied using the procedure outlined in Fig. 3. Different quantities of $CaCO_3$ powder are mixed together with small amount of water and poured into the 5 × 5 cm^2 square frame. To prevent the mixture from spilling, a rubber insulation layer is used and the frame is pressed using two clamps. The sample is left at room temperature until the water evaporates (around 16 h), leaving only the $CaCO_3$ layer on the given area. The preparation is considered satisfactory if the contaminant layer adheres to the surface of the sample, as it is placed in the vertical position for the full-field measurement. The sample is prepared with $CaCO_3$ masses of 0.067, 0.125, 0.25, 0.5 and 1 g, resulting in layers of different thicknesses.

After the contamination is applied to the plate, the full-field measurements are performed on the area of 140 × 120 mm^2 with spatial sampling of 2 mm, resulting in a mesh of 71 × 61 measurement points. Excitation is realized using a 100 ms frequency sweep in the range between 1 and 300 kHz, with an amplitude of 10 Vpp. The wavefield is also measured by a second transducer on the other side of the $CaCO_3$ layer. After removing the contaminant from the surface of the plate, the full-field and inter-transducer signals are acquired to obtain baseline data of the clean sample. After that, the new contamination level is applied to the same sample, using the aforementioned procedure. The data sets obtained from the measurements are denoted as $\mathbf{DataC}_m^{b/c}$, where m is the mass of deposited $CaCO_3$ and **b/c** indicates signals from either the clean sample (baseline) **b** or with contamination **c**.

4. Estimation results from the polypropylene sample

4.1. Estimation of viscoelastic properties

In the first step, the elastic properties of the samples are estimated using the procedure described in Section 2.1. The procedure is based on the frequency–wavenumber dispersion curves $U(k_x, k_y, \omega)$ calculated from the entire full-field **DataA** $u(x, y, t)$ (snapshot in Fig. 4(a)) using 3D Fourier Transform (see [42] for details). The dispersion curves along the Y axis ($U(0, k_Y, \omega)$) in Fig. 4(b) show multiple modes, with the most significant contribution of A0, S0 and A1. Furthermore, the initial examination of the dispersion curves in the 2D k-space (Fig. 4(c)) shows, that the properties in the XY plane within the examined frequency range are almost isotropic, as the wavenumbers in different directions do not vary by more than 10%. On the other hand, it is impossible to obtain a correct fit with a purely isotropic material model. Therefore, a transversely isotropic model is assumed, with the axis of symmetry oriented in the through-thickness direction of the plate (as depicted in Fig. 4(d)). The density of the plate is assumed to be 950 kg/m^3 according to the manufacturer's data. Therefore, there are five independent unknown parameters with real values in the model: E_1, E_2, ν_{13}, ν_{12} and G_{12}. The initial parameter ranges as well as the settings for the genetic algorithm are presented in the Tables 1 and 2, respectively. The range of parameter space was chosen based on the manufacturer's data, which provided the order of magnitude for different parameters. Additionally, a stopping criterion for the genetic algorithm was defined in the form of a maximum number of generations with the same cost function value. For the inversion procedure, the stopping criterion was set to 150 consecutive values and it was reached before the maximum number of iterations, indicating convergence of the algorithm. The theoretical dispersion curves obtained from the inversion scheme are presented in Fig. 4(e) (red curves), showing a very good match with the experimental dispersion curves, especially for low order modes. The full list of estimated elastic parameters is included in the first two rows of Table 4. The parameters are presented as coefficients of the stiffness matrix C in the Voigt notation.

In the next step, the frequency dependent attenuation is estimated using the Laplacian technique outlined in Section 2.2 with data **DataA**

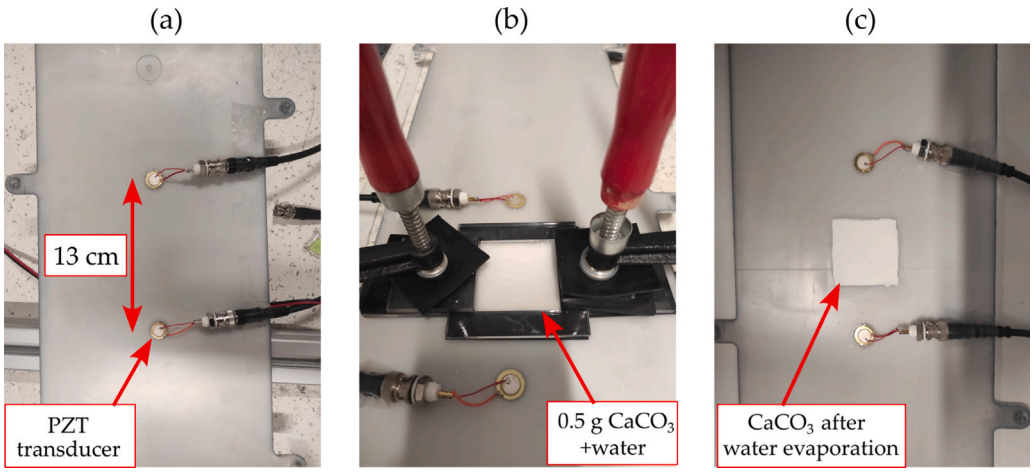

Fig. 3. Deposition of the calcium carbonate ($CaCO_3$) layer on the Polypropylene plate: (a) clean plate with glued PZT transducers, (b) 5 × 5 cm^2 frame with $CaCO_3$ solution fixed on the plate, (c) $CaCO_3$ after the water evaporated.

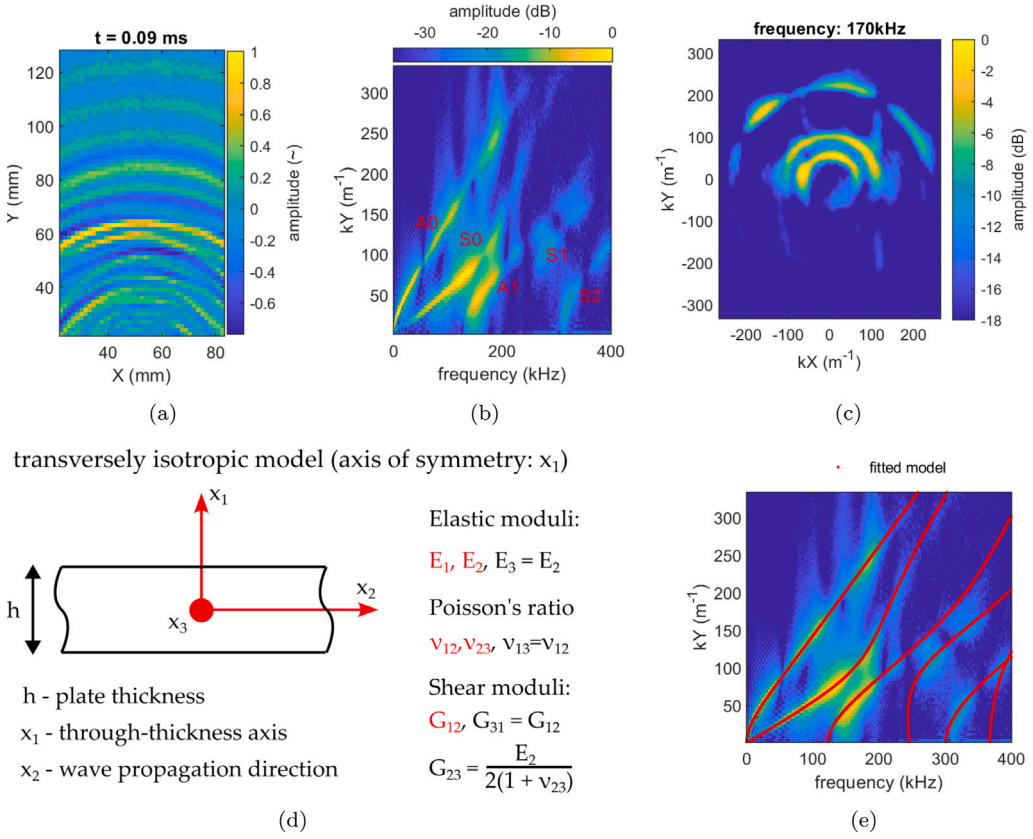

Fig. 4. (a) Space–time snapshot of **DataA**. (b) Frequency–wavenumber dispersion curves from **DataA**. (c) 2D wavenumber dispersion curves from **DataA** for frequency 170 kHz (d) Geometry of the transversely isotropic model with independent parameters indicated by a red color. (e) Theoretical dispersion curves of elastic model compared with the experimental curves.

(snapshot in Fig. 5(a)). The estimation is performed for the three most significant modes, according to the frequency–wavenumber spectrum in Fig. 4(b): A0, S0 and A1. Each of these modes is filtered around a manually selected central wavenumber k_c, using the mode filter $W(k,\omega)$ defined by Eq. (2) with $B_m = 15$ m^{-1}. After calculating the attenuation map $\alpha(x,\omega)$ according to Eq. (7), for each frequency ω a median filter with window size of 3 × 3 pixels is used to remove measurement artefacts. An example of an attenuation map obtained for the mode A0 is presented in Fig. 5(b). The local attenuation map is slightly nonuniform, but at the bottom part there is a circular area with significantly different attenuation. The estimates in that area result from near-source artefacts due to filtration operations. The mean attenuation for a given frequency is taken from the area indicated by the red rectangle (including a total of 1496 values) in Figs. 5(a) and 5(b), excluding the zone with artefacts. After calculating the attenuation map for every mode (A0, S0 and A1) and for frequencies in the range between 20 and 200 kHz, the plot of the modal attenuation is obtained, as shown in Fig. 5(c) (blue, red and green curves). The frequency range of estimated values is narrower than the excitation frequency (1–400 kHz) due to high attenuation of the structure, excitability characteristics of the transducer and limited sensitivity of the measurement system. This results in an insufficient SNR for frequencies above 200 kHz, leading

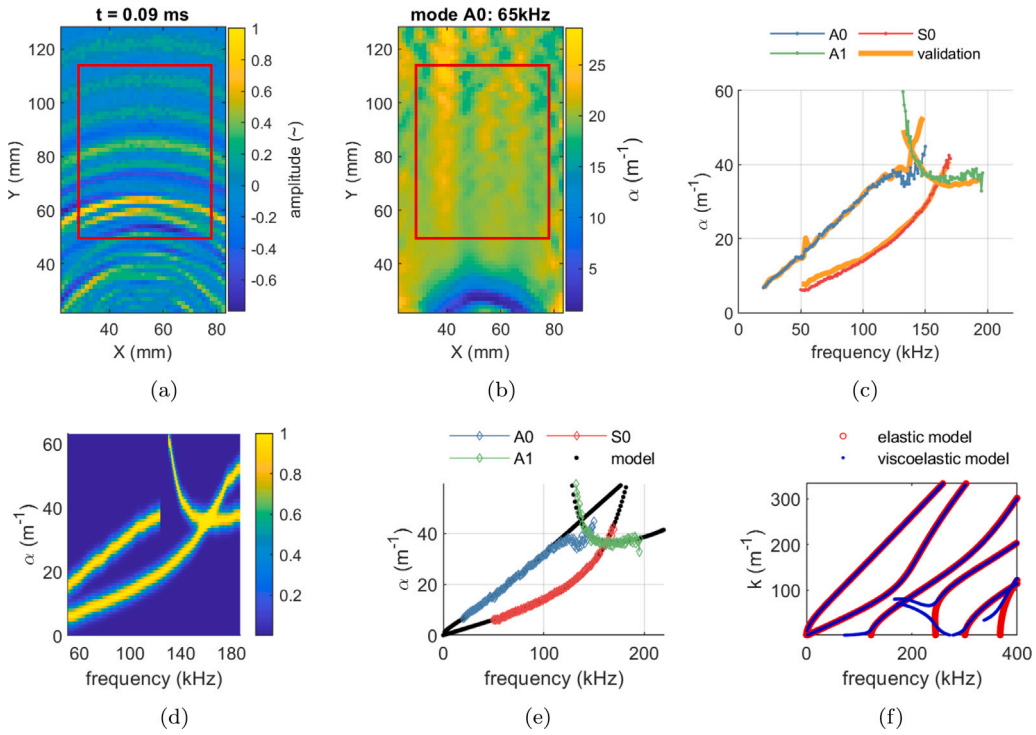

Fig. 5. (a) Snapshot of the wavefield from **DataA**. (b) Local attenuation map for mode A0 and central frequency of 65 kHz. (c) Comparison between modal attenuation obtained using Laplacian method (blue, red and green) and using curve fitting to the exponential decay equation (orange). (d) 2D mask based on attenuation curves in figure (c) with added Gaussian window. (e) Comparison between experimental attenuation (blue, red, green) and imaginary part of estimated viscoelastic model (black). (f) Theoretical dispersion curves calculated using elastic (red) and viscoelastic (blue) model.

Table 1
Value ranges assumed for the estimation of elastic parameters using genetic algorithm. Thickness h and density ρ are assumed constant.

Parameter	E_1, $E_2 = E_3$	ν_{23}, $\nu_{13} = \nu_{12}$	G_{12}	ρ	h
Values	0.5–4 GPa	0.1–0.45	0.125–1.5 GPA	950 kg/m^3	3.4 mm

to poor estimation quality. Therefore, only the attenuation estimates up to 200 kHz are included in the figure. To validate this result, the attenuation was also estimated using a method based on fitting the formula of exponential wave decay with distance, as outlined in [43]. The result of applying the exponential wave decay method to individual Lamb modes is shown as an orange plot in Fig. 5(c). The curves obtained using the Laplacian and the curve fitting to the exponential decay formula match very well.

Knowing the elastic parameters C and attenuation α, the viscous parameters C' are estimated by fitting the imaginary part of theoretical dispersion curves to the attenuation plots in Fig. 5(c), using the approach described in Section 2.2. In order to directly apply the inversion procedure outlined in Fig. 1, a 2D mask is created based on attenuation curves, with Gaussian window applied at each frequency. The resulting mask is presented in Fig. 5(d). This mask is then multiplied with the mask obtained from imaginary part of theoretical dispersion curves and subsequently summing all the values, resulting in the fitness value F. The viscous parameter ranges in the inversion procedure are assumed as shown in Table 3. Additionally, the dispersion curves are calculated using parameters C listed in the two first rows of Table 4, as well as thickness and density in Table 1. The settings of genetic algorithm are listed in Table 2, same as in the previous inversions. The inversion procedure for viscous parameters ended prematurely, as the stop criterion of 150 consecutive fitness values with unchanging best fit value was reached. The estimated viscous parameters with best fitness are presented in the third and fourth rows of Table 4. The imaginary part of dispersion curves (black points) for obtained viscous parameters match the attenuation curves (blue, red and green points) very well, as depicted in Fig. 5(e). The real part of the dispersion curves calculated using a full viscoelastic model C_c is presented in Fig. 5(f), and compared to the dispersion curves obtained with just the elastic components C. For a more clear comparison, the frequency–wavenumber points with very high imaginary part are removed from the plot. In the given frequency range, the curves obtained with the viscoelastic model match the elastic model very well. The most significant differences between the two models occur at the points with highest attenuation, e.g. close to the cutoff frequencies.

4.2. $CaCO_3$ parameters estimation

The Laplacian algorithm was applied to all data sets with $CaCO_3$ of **DataC**$_m$ to estimate local wavenumbers of the contamination area. Examples of wavenumber maps obtained for baseline data **DataC**$_1^b$ calculated using the modes A0 and A1 are presented in Figs. 6(a) and 6(b) respectively, and maps for the same modes with added contamination from data **DataC**$_1^c$ (1 g of $CaCO_3$) are shown in Figs. 6(c) and 6(d). The baseline maps in Figs. 6(a) and 6(b) show nonuniform wavenumber estimates, resulting from material inhomogeneity and slight anisotropy in the XY plane. The wavenumber values in the baseline maps do not differ by more than 10%, which is consistent with initial examination of the anisotropy of the $U(k_x, k_y)$ dispersion curves, as described in Section 4.1. Looking at the maps with 1 g of $CaCO_3$, we can see a clear increase in local wavenumber in the central area, where the contamination was applied. Therefore, local dispersion properties of individual modes are clearly affected by adding a layer of contaminant. To illustrate these changes, for each frequency the local wavenumber values are averaged from the area indicated by the red rectangle. The rectangle is chosen to be smaller than the extent of the contamination to avoid spurious wavenumber artefacts resulting from effects at the edge of the contaminant (e.g. due to wave scattering). The resulting frequency–wavenumber pairs are presented in Fig. 7(a), as colored

Table 2
Settings of the genetic algorithm.

Setting name	Mutation probability	Crossover probability	Tournament probability	Mutation scale	Generations	Population size	Stop criterion
Setting value	0.2	0.7	0.4	0.1	1000	40	150

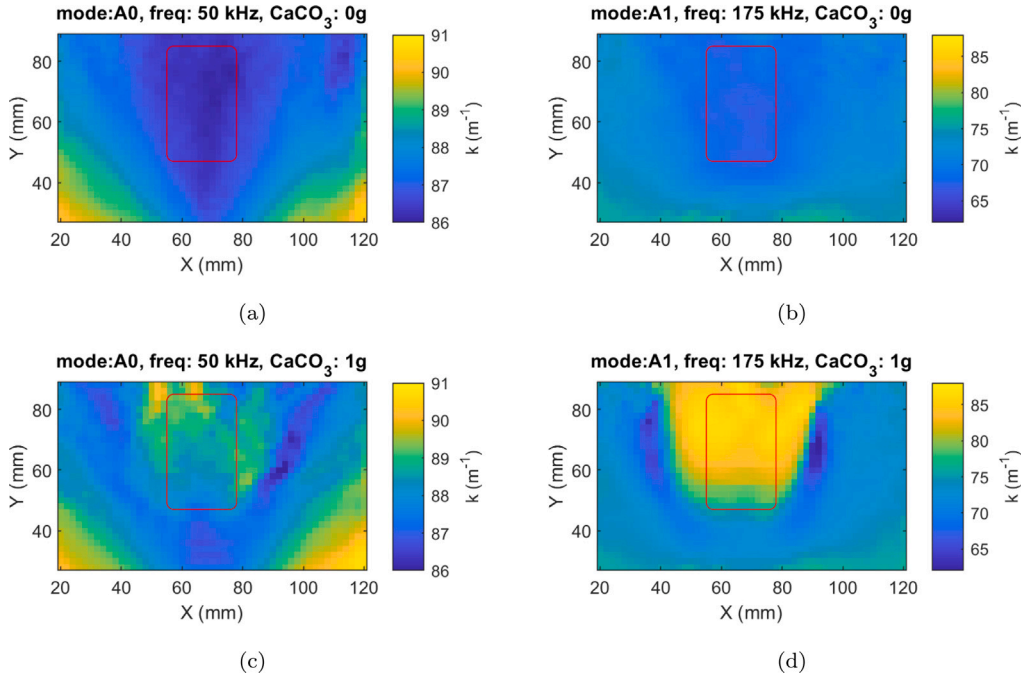

Fig. 6. Local wavenumber maps calculated using the Laplacian method for (a,b) $\mathbf{DataC}_1^b$ and (c,d) $\mathbf{DataC}_1^c$.

Table 3
Value ranges assumed for the estimation of viscous parameters using genetic algorithm.

Parameter	C'_{11}	$C'_{22} = C'_{33}$	C'_{23}	$C'_{12} = C'_{13}$	$C'_{55} = C'_{66}$
Value (GPa)	0.1–0.3	0.1–0.3	0.05–0.15	0.05–0.15	0.05–0.15

Table 4
The elastic C and viscous C' parameters estimated for polypropylene plate.

Elastic parameters	C_{11}	$C_{22} = C_{33}$	$C_{12} = C_{13}$	C_{23}	$C_{55} = C_{66}$
Value (GPa)	3.974	5.67	3.004	3.886	0.66
Viscous parameters	C'_{11}	$C'_{22} = C'_{33}$	$C'_{12} = C'_{13}$	C'_{23}	$C'_{55} = C'_{66}$
Value (GPa)	1.746	0.288	0.095	0.146	0.06

dash-circle plots. It is evident from the plots, that the addition of contamination affects all the modes, but the increase in wavenumber values is most evident for the A1 mode (as shown on the close-up in Fig. 7(b)). Similarly to the attenuation estimation procedure for the polypropylene plate, the SNR of higher frequency components is not high enough to obtain accurate estimates of local wavenumbers. Therefore, only the wavenumber components lower than 200 kHz were included. In order to estimate the properties of the $CaCO_3$ contamination, the inversion procedure is applied once more, this time assuming a simplified isotropic model of $CaCO_3$. For the calculation of dispersion curves in the inversion procedure, the bi-layer plate model is used instead of a single-layer model. The parameters of $CaCO_3$ are treated as unknowns, namely: Young's Modulus E, Poisson's ratio ν and density ρ. For the polypropylene substrate, the elastic properties estimated in Section 4.1 are used and the viscous parameters are neglected due to their small influence on the dispersion curves in the given frequency range. The thickness of the $CaCO_3$ layer for the calculation of theoretical dispersion curves is derived from the mass, estimated density and the assumption, that the layer was distributed evenly over the area of 5×5 cm^2 during the sample preparation, obtaining a roughly uniform density. The initial settings of the genetic algorithm are the same as presented in Table 2. The stopping criterion value was again set to 150 consecutive generations with the same cost value and the algorithm converged before reaching maximum number of iterations.

Using this inversion procedure, the following properties of the $CaCO_3$ are obtained: $E = 0.972$ GPa, $\nu = 0.09$ and $\rho = 1102$ kg/m^3. It must be stressed, however, that the Poisson's ratio does not significantly influence the dispersion curves in this frequency range, and should be considered unknown. However, despite not fully representing the physical properties of the layer, this model can serve as a way to predict the sensitivity of the Lamb waves to contamination during monitoring. Dispersion curves calculated using these properties are demonstrated in Figs. 7(a) and 7(b) as grey scale lines. The curves are calculated for thickness values corresponding to various mass quantities distributed over the area of 5×5 cm^2. Presenting the theoretical curves for mass rather than the thickness makes them easier to compare with the experimental data. Figs. 7(a) and 7(b) show a very good match between experimental data and the model. Fig. 7(c) presents the frequency-group velocity dispersion curves, which indicates how the time-of-flight of transmitted Lamb modes would be affected by a $CaCO_3$ layer. The plots are calculated for thickness values ranging from 0 to 0.363 mm, which are equivalent to the masses in Fig. 7(a) distributed over area of 5×5 cm^2.

Using the bi-layer plate model, we performed a sensitivity analysis of Lamb waves to surface contamination in the form of $CaCO_3$ on the surface of a polypropylene plate. To that end, the partial derivative of each mode with respect to the contaminant thickness ($\frac{dV}{dH}$) is represented as a function of frequency in Figs. 7(d)–7(f). High values of the derivative indicate, that the group velocity plots are more significantly affected by change in the thickness of the contaminant layer. Based

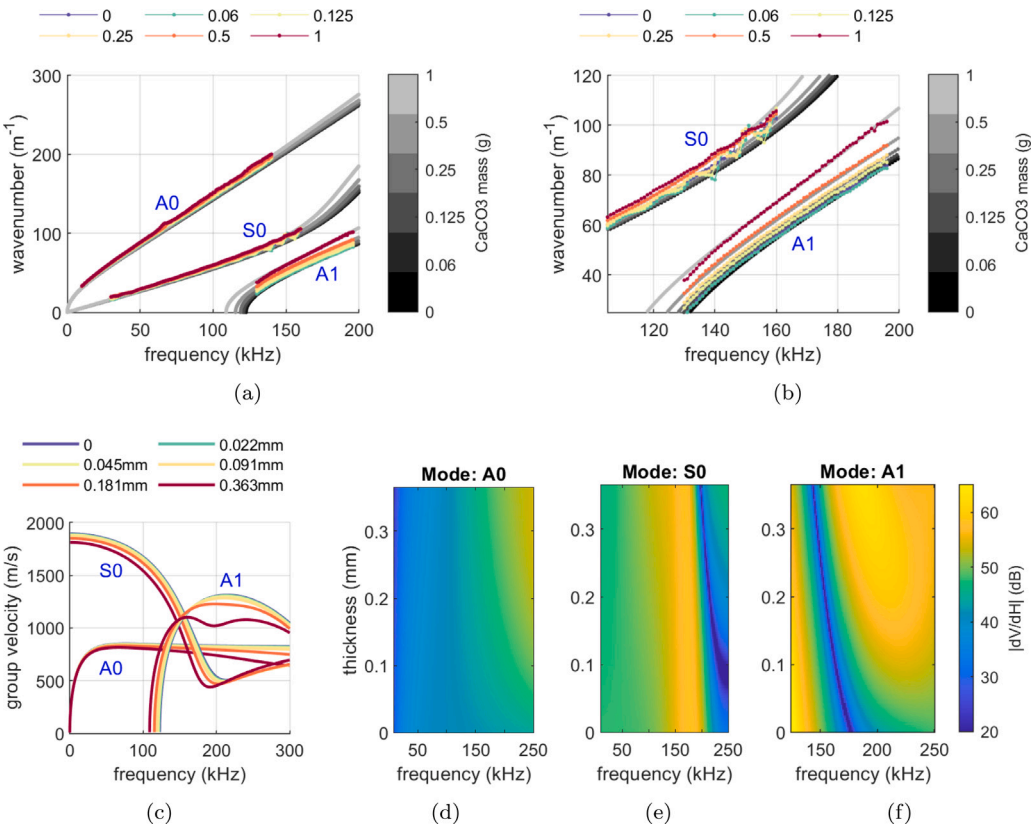

Fig. 7. (a,b) Comparison between local wavenumber estimates from the contamination area in $\mathbf{DataC}_{0-1}$ and dispersion curves from fitted bi-layer model. (c) Theoretical group velocity plots for different thickness of $CaCO_3$. Sensitivity analysis based on partial derivative of group velocities over thickness of $CaCO_3$ layer ($\frac{dV}{dH}$) for modes (d) A0, (e) S0, (f) A1.

on these sensitivity plots, it is possible to select the most appropriate modes and frequency ranges for the detection of surface contaminants using Lamb waves.

5. Discussion and the application to monitoring

The sensitivity plots in Figs. 7(d)–7(f) show that modes A0 and S0 are weakly affected by the contaminant layer below 120 kHz, as their group velocities do not change significantly with respect to the clean plate. The sensitivity of A0 mode becomes significant at frequencies higher than 200 kHz, as the group velocity dispersion curves begin to diverge more significantly. However, due to the high attenuation of polypropylene, it may not be possible to transmit these frequencies between transducers over longer distances. The S0 mode appears to be sensitive to the contamination layer between 150 kHz and 200 kHz. In this frequency range, changes in the thickness of the $CaCO_3$ result in a more pronounced divergence of the dispersion curves with respect to a clean plate. For higher frequencies, the S0 plots converge again, as shown in Fig. 7(c), resulting in a significant sensitivity drop in Fig. 7(e) (dark-blue colored region). For mode A1, the sensitivity values are overall the highest, apart from the narrow frequency bandwidth between 150 kHz and 170 kHz, which corresponds to the crossing of the dispersion curves (see Fig. 7(c)). Overall, the A1 maintains high sensitivity near the cutoff frequency and for frequencies higher than the crossing point. However, similar to A0 mode, it would be difficult to propagate and detect higher frequency components of mode A1 over longer distances due to high attenuation of the substrate, as evident from Fig. 5(c), so the useful frequency of A1 is in the range from 125 kHz to 200 kHz.

The sensitivity analysis presented in Fig. 7 can be used to design the monitoring strategy using a network of transducers. To demonstrate the validity of the performed analysis, the signals obtained from the inter-transducer measurements from datasets $\mathbf{DataC}_{0.06-1}$ are processed. These inter-transducer measurements used the same excitation as full-field measurements, meaning that modes A0, S0 and A1 will be recorded by a receiving transducer. Signals obtained from the measurement $\mathbf{DataC_{0.25}}$ are presented in Fig. 8(a). The signals were then filtered to two frequency bands: 0–100 Hz and 120–200 kHz. The first band is expected to contain modes with weak sensitivity to surface contaminations (A0 and S0), while the second band will contain more sensitive modes (S0 and A1). For frequencies 0 to 100 kHz (Fig. 8(b)), the differences between the baseline $\mathbf{DataC}^b_{0.25}$ and the signal from the sample with contamination $\mathbf{DataC}^c_{0.25}$ are very minimal. For frequencies 120 to 200 kHz (Fig. 8(c)), a noticeable time shift appears between $\mathbf{DataC}^b_{0.25}$ and $\mathbf{DataC}^c_{0.25}$. In order to quantify these differences, a Difference Index (DI) [44] is calculated between baselines and signals from samples with contaminations for all the deposited masses $\mathbf{DataC}_{0.06-1}$, according to the formula:

$$DI = \frac{\sum_t (Y(t) - X(t))^2}{\sum_t (X(t))^2}, \tag{8}$$

where $X(t)$ is the envelope of the baseline signal and $Y(t)$ is the envelope of a signal from the sample with contamination. The DI is calculated separately for the bands 0–100 kHz (Fig. 8(d)) and 120–200 kHz (Fig. 8(e)). The DI value for a clean plate is an average of DI's calculated between different baseline signals, acquired before and after depositing every $CaCO_3$ layer. Therefore, from six baseline signals five DI values are calculated. Moreover, using these baseline DI's a simple detection threshold is established as a mean value plus three times standard deviation. These detection thresholds are plotted on Figs. 8(d) and 8(e) as dashed red lines. As evident from the plots, the DI's for the band 0–100 kHz exceed the detection threshold only at 0.5 and 1 g mass. On the other hand, the DI's for the band 120–200 kHz exceed the threshold starting from 0.125 g. Therefore, the sensitivity to $CaCO_3$ is

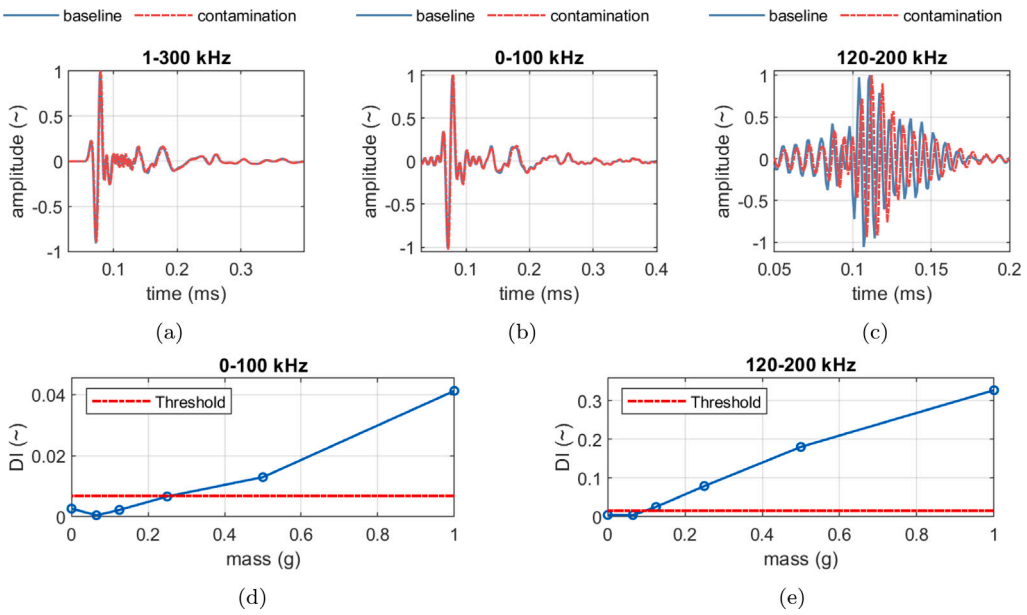

Fig. 8. (a) Time signals with and without contamination from dataset **Data$C_{0.25}$**. Signals filtered for the frequency band (b) 0–100 kHz and (c) 120–200 kHz. Signal difference index plotted versus mass of deposited $CaCO_3$ for signals filtered to (d) 0–100 kHz and (e) 120–200 kHz.

much higher for 120–200 kHz, which is consistent with the sensitivity analysis presented in Fig. 7.

6. Conclusions

An inversion scheme was applied to estimate viscoelastic parameters of the polypropylene plate based on full-field measurements of Lamb waves. A transversely isotropic material model with the axis of symmetry in the through-thickness direction provided a good approximation of the plate's properties. In the next step, a simplified model of $CaCO_3$ contamination was proposed based on the local wavenumber estimates calculated using the Laplacian of the full-field measurement data. Based on the estimated effective properties, the sensitivity study was performed to determine the most suitable Lamb modes and frequency bands for the detection of $CaCO_3$ contamination. Finally, simple through-transmission measurements using two PZT transducers were performed to confirm the validity of the sensitivity study. The results of these measurements were consistent with the models for the polypropylene plate with $CaCO_3$ contamination.

These results can be used to determine the minimum amount of contamination that can be detected using a monitoring system. Due to high material attenuation the frequency bandwidth of Lamb waves that could be used for characterization is limited. As a result, the assumed material models for both the polypropylene plate and the $CaCO_3$ contamination are simplified, and may not represent ground truth, especially the properties of $CaCO_3$. However, this model correctly predicts the sensitivity of Lamb waves in the frequencies below 200 kHz, which is sufficient for a monitoring system working in the low-power consumption regime. In further work, the system could be used to not only detect but also to localize the contamination, e.g. using a tomography setup.

CRediT authorship contribution statement

Jakub Spytek: Writing – original draft, Validation, Software, Methodology, Investigation, Formal analysis, Data curation. **Daniel A. Kiefer:** Writing – review & editing, Software. **Ros Kiri Ing:** Supervision, Resources, Project administration, Funding acquisition, Conceptualization. **Claire Prada:** Writing – review & editing, Supervision, Project administration, Funding acquisition, Conceptualization. **Jérôme Grando:** Supervision, Resources, Conceptualization. **Julien de Rosny:** Writing – review & editing, Supervision, Resources, Project administration, Funding acquisition, Conceptualization.

Declaration of competing interest

The authors declare the following financial interests/personal relationships which may be considered as potential competing interests: Jakub Spytek reports financial support was provided by Plastic Omnium.

Acknowledgment

The authors would like to acknowledge Nicolas Bochud for the help with implementation of genetic algorithm in the inversion procedure.

Appendix. Engineering constants to elastic matrix conversion

The elastic stiffness matrix C_{ij} can be expressed with respect to the engineering constants, namely Young's modulus E_i, Poisson's ratio ν_{ij}, and shear modulus G_{ij}, where subscripts i and j indicate axes in the Cartesian coordinates system x_1, x_2, x_3 (i.e., $i, j = 1, 2, 3$). Assuming an orthotropic material model with 9 independent parameters, the relationship between engineering constants and coefficients of the matrix C_{ij} is given by the following equations [40]:

$$
\begin{aligned}
C_{11} &= \frac{(1-\nu_{23}\nu_{32})E_1}{N} \\
C_{22} &= \frac{(1-\nu_{13}\nu_{31})E_2}{N} \\
C_{33} &= \frac{(1-\nu_{12}\nu_{21})E_3}{N} \\
C_{12} &= \frac{(\nu_{21}+\nu_{31}\nu_{23})E_1}{N} = \frac{(\nu_{12}+\nu_{32}\nu_{13})E_2}{N} \\
C_{13} &= \frac{(\nu_{31}+\nu_{21}\nu_{32})E_1}{N} = \frac{(\nu_{13}+\nu_{12}\nu_{23})E_3}{N} \\
C_{23} &= \frac{(\nu_{32}+\nu_{12}\nu_{31})E_2}{N} = \frac{(\nu_{23}+\nu_{21}\nu_{13})E_3}{N} \\
C_{44} &= G_{23}, \quad C_{55} = G_{31}, \quad C_{66} = G_{12}
\end{aligned}
\tag{A.1}
$$

where N is a factor given by:

$$
N = 1 - \nu_{12}\nu_{21} - \nu_{23}\nu_{32} - \nu_{31}\nu_{13} - 2\nu_{21}\nu_{32}\nu_{13} \tag{A.2}
$$

The material with transverse isotropy consists of an axis of symmetry x_1 orthogonal to the plane of isotropy x_2, x_3. This material symmetry results in five independent engineering coefficients: E_1, E_2, ν_{12}, ν_{23} and G_{12}. The corresponding coefficients of the C_{ij} matrix are given as follows:

$$
\begin{aligned}
C_{11} &= \frac{(1-\nu_{23}\nu_{32})E_1}{N} \\
C_{22} &= \frac{(1-\nu_{12}\nu_{21})E_2}{N} = C_{33} \\
C_{12} &= \frac{(\nu_{21}+\nu_{21}\nu_{23})E_1}{N} = C_{13} \\
C_{23} &= \frac{(\nu_{32}+\nu_{12}\nu_{21})E_2}{N} \\
C_{55} &= G_{12} = C_{66} \\
C_{44} &= 0.5(C_{22}-C_{23})
\end{aligned}
\tag{A.3}
$$

Data availability

The data that has been used is confidential.

References

[1] M. Holder, S. Hellwig, H. Winner, Real-time pose graph SLAM based on radar, in: 2019 IEEE Intelligent Vehicles Symposium, IV, Vol. 2019-June, IEEE, 2019, pp. 1145–1151, http://dx.doi.org/10.1109/IVS.2019.8813841, URL https://ieeexplore.ieee.org/document/8813841/.

[2] W.H. Leong, W.J. Staszewski, B.C. Lee, F. Scarpa, Structural health monitoring using scanning laser vibrometry: III. Lamb waves for fatigue crack detection, Smart Mater. Struct. 14 (6) (2005) 1387–1395, http://dx.doi.org/10.1088/0964-1726/14/6/031, URL https://iopscience.iop.org/article/10.1088/0964-1726/14/6/031.

[3] M. Philibert, K. Yao, M. Gresil, C. Soutis, Lamb waves-based technologies for structural health monitoring of composite structures for aircraft applications, Eur. J. Mater. 2 (1) (2022) 436–474, http://dx.doi.org/10.1080/26889277.2022.2094839, URL https://www.tandfonline.com/doi/full/10.1080/26889277.2022.2094839.

[4] G.M. Ramalho, A.M. Lopes, L.F. da Silva, Structural health monitoring of adhesive joints using Lamb waves: A review, Struct. Control Health Monit. 29 (1) (2022) 1–22, http://dx.doi.org/10.1002/stc.2849.

[5] X. Zhao, R.L. Royer, S.E. Owens, J.L. Rose, Ultrasonic Lamb wave tomography in structural health monitoring, Smart Mater. Struct. 20 (10) (2011) 105002, http://dx.doi.org/10.1088/0964-1726/20/10/105002, URL https://iopscience.iop.org/article/10.1088/0964-1726/20/10/105002.

[6] P. Huthwaite, F. Simonetti, High-resolution guided wave tomography, Wave Motion 50 (5) (2013) 979–993, http://dx.doi.org/10.1016/j.wavemoti.2013.04.004, URL https://linkinghub.elsevier.com/retrieve/pii/S0165212513000759.

[7] J. Rao, M. Ratassepp, Z. Fan, Investigation of the reconstruction accuracy of guided wave tomography using full waveform inversion, J. Sound Vib. 400 (2017) 317–328, http://dx.doi.org/10.1016/j.jsv.2017.04.017, URL https://linkinghub.elsevier.com/retrieve/pii/S0022460X17303231.

[8] Z.-B. Yang, M.-F. Zhu, Y.-F. Lang, X.-F. Chen, FRF-based lamb wave phased array, Mech. Syst. Signal Process. 166 (August 2021) (2022) 108462, http://dx.doi.org/10.1016/j.ymssp.2021.108462, URL https://linkinghub.elsevier.com/retrieve/pii/S0888327021008086.

[9] P. Wang, W. Zhou, Y. Bao, H. Li, Ice monitoring of a full-scale wind turbine blade using ultrasonic guided waves under varying temperature conditions, Struct. Control Health Monit. 25 (4) (2018) e2138, http://dx.doi.org/10.1002/stc.2138, URL https://onlinelibrary.wiley.com/doi/10.1002/stc.2138.

[10] X. Zhao, J.L. Rose, Ultrasonic guided wave tomography for ice detection, Ultrasonics 67 (2016) 212–219, http://dx.doi.org/10.1016/j.ultras.2015.12.005, URL https://linkinghub.elsevier.com/retrieve/pii/S0041624X1500311X.

[11] J.H. Tam, Z.C. Ong, Z. Ismail, B.C. Ang, S.Y. Khoo, Identification of material properties of composite materials using nondestructive vibrational evaluation approaches: A review, Mech. Adv. Mater. Struct. 24 (12) (2017) 971–986, http://dx.doi.org/10.1080/15376494.2016.1196798, URL https://www.tandfonline.com/doi/full/10.1080/15376494.2016.1196798.

[12] A. Martens, M. Kersemans, J. Daemen, E. Verboven, W. Van Paepegem, S. Delrue, K. Van Den Abeele, Characterization of the orthotropic viscoelastic tensor of composites using the Ultrasonic Polar Scan, Compos. Struct. 230 (April) (2019) 111499, http://dx.doi.org/10.1016/j.compstruct.2019.111499, URL https://linkinghub.elsevier.com/retrieve/pii/S0263822319311274.

[13] A.H. Orta, M. Kersemans, K. Van Den Abeele, On the identification of orthotropic elastic stiffness using 3D guided wavefield data, Sensors 22 (14) (2022) 5314, http://dx.doi.org/10.3390/s22145314, URL https://www.mdpi.com/1424-8220/22/14/5314.

[14] S. Wang, Z. tao Luo, J. Jing, Z. hao Su, X. kai Wu, Z. hua Ni, H. Zhang, Real-time determination of elastic constants of composites via ultrasonic guided waves and deep learning, Measurement 200 (2022) 111680, http://dx.doi.org/10.1016/j.measurement.2022.111680, URL https://linkinghub.elsevier.com/retrieve/pii/S0263224122008880.

[15] Q. Chen, K. Xu, D. Ta, High-resolution Lamb waves dispersion curves estimation and elastic property inversion, Ultrasonics 115 (March) (2021) 106427, http://dx.doi.org/10.1016/j.ultras.2021.106427, URL https://linkinghub.elsevier.com/retrieve/pii/S0041624X21000664.

[16] X. Gao, Y. Tian, J. Jiao, C. Li, J. Gao, Non-destructive measurements of thickness and elastic constants of plate structures based on Lamb waves and particle swarm optimization, Measurement 204 (August) (2022) 111981, http://dx.doi.org/10.1016/j.measurement.2022.111981, URL https://linkinghub.elsevier.com/retrieve/pii/S0263224122011770.

[17] A.H. Orta, M. Kersemans, N.B. Roozen, K. Van Den Abeele, Characterization of the full complex-valued stiffness tensor of orthotropic viscoelastic plates using 3D guided wavefield data, Mech. Syst. Signal Process. 191 (February) (2023) 110146, http://dx.doi.org/10.1016/j.ymssp.2023.110146, URL https://linkinghub.elsevier.com/retrieve/pii/S0888327023000535.

[18] J. Vishnuvardhan, C.V. Krishnamurthy, K. Balasubramaniam, Blind inversion method using Lamb waves for the complete elastic property characterization of anisotropic plates, J. Acoust. Soc. Am. 125 (2009) 761–771, http://dx.doi.org/10.1121/1.3050253.

[19] N. Bochud, J. Laurent, F. Bruno, D. Royer, C. Prada, Towards real-time assessment of anisotropic plate properties using elastic guided waves, J. Acoust. Soc. Am. 143 (2) (2018) 1138–1147, http://dx.doi.org/10.1121/1.5024353, URL https://pubs.aip.org/jasa/article/143/2/1138/606472/Towards-real-time-assessment-of-anisotropic-plate.

[20] P. Kudela, M. Radzienski, P. Fiborek, T. Wandowski, Elastic constants identification of fibre-reinforced composites by using guided wave dispersion curves and genetic algorithm for improved simulations, Compos. Struct. 272 (March) (2021) 114178, http://dx.doi.org/10.1016/j.compstruct.2021.114178, URL https://linkinghub.elsevier.com/retrieve/pii/S0263822321006401.

[21] H. Chen, F. Ling, W. Zhu, D. Sun, X. Liu, Y. Li, D. Li, K. Xu, Z. Liu, D. Ta, Waveform inversion for wavenumber extraction and waveguide characterization using ultrasonic Lamb waves, Meas. 207 (2023) http://dx.doi.org/10.1016/j.measurement.2022.112360.

[22] R. Cui, F. Lanza di Scalea, On the identification of the elastic properties of composites by ultrasonic guided waves and optimization algorithm, Compos. Struct. 223 (February) (2019) 110969, http://dx.doi.org/10.1016/j.compstruct.2019.110969.

[23] J. Foiret, J.-G. Minonzio, C. Chappard, M. Talmant, P. Laugier, Combined estimation of thickness and velocities using ultrasound guided waves: a pioneering study on in vitro cortical bone samples, IEEE Trans. Ultrason. Ferroelectr. Freq. Control 61 (2014) 1478–1488, http://dx.doi.org/10.1109/TUFFC.2014.3062, URL https://ieeexplore.ieee.org/document/6882946.

[24] S. Johannesmann, L. Claes, B. Henning, Lamb wave based approach to the determination of elastic and viscoelastic material parameters, tm - Tech. Mess. 88 (s1) (2021) s28–s33, http://dx.doi.org/10.1515/teme-2021-0070, URL https://www.degruyter.com/document/doi/10.1515/teme-2021-0070/html.

[25] A.H. Orta, J.D. Boer, M. Kersemans, C. Vens, K.V.D. Abeele, Machine learning-based orthotropic stiffness identification using guided wavefield data, Measurement 214 (2023) 112854, http://dx.doi.org/10.1016/j.measurement.2023.112854, URL https://linkinghub.elsevier.com/retrieve/pii/S0263224123004189.

[26] M. Ponschab, D.A. Kiefer, S.J. Rupitsch, Simulation-based characterization of mechanical parameters and thickness of homogeneous plates using guided waves, IEEE Trans. Ultrason. Ferroelectr. Freq. Control 66 (12) (2019) 1898–1905, http://dx.doi.org/10.1109/TUFFC.2019.2933699, URL https://ieeexplore.ieee.org/document/8790793/.

[27] E.B. Flynn, S.Y. Chong, G.J. Jarmer, J.-R. Lee, Structural imaging through local wavenumber estimation of guided waves, NDT E Int. 59 (2013) 1–10, http://dx.doi.org/10.1016/j.ndteint.2013.04.003, URL https://linkinghub.elsevier.com/retrieve/pii/S0963869513000595.

[28] M.D. Rogge, C.A. Leckey, Characterization of impact damage in composite laminates using guided wavefield imaging and local wavenumber domain analysis, Ultrasonics 53 (7) (2013) 1217–1226, http://dx.doi.org/10.1016/j.ultras.2012.12.015, URL https://linkinghub.elsevier.com/retrieve/pii/S0041624X13000607.

[29] F.A. Purcell, M. Eaton, M. Pearson, R. Pullin, Non-destructive evaluation of isotropic plate structures by means of mode filtering in the frequency-wavenumber domain, Mech. Syst. Signal Process. 142 (2020) 106801, http://dx.doi.org/10.1016/j.ymssp.2020.106801, URL https://linkinghub.elsevier.com/retrieve/pii/S0888327020301874.

[30] J.Y. Jeon, D. Kim, G. Park, E. Flynn, T. Kang, S. Han, 2D-wavelet wavenumber filtering for structural damage detection using full steady-state wavefield laser scanning, NDT E Int. 116 (August) (2020) 102343, http://dx.doi.org/10.1016/j.ndteint.2020.102343.

[31] O. Mesnil, C.A. Leckey, M. Ruzzene, Instantaneous and local wavenumber estimations for damage quantification in composites, Struct. Health Monit. 14 (3) (2015) 193–204, http://dx.doi.org/10.1177/1475921714560073, URL http://shm.sagepub.com/cgi/doi/10.1177/1475921714560073 http://journals.sagepub.com/doi/10.1177/1475921714560073.

[32] J. Segers, S. Hedayatrasa, G. Poelman, W. Van Paepegem, M. Kersemans, Self-reference broadband local wavenumber estimation (SRB-LWE) for defect assessment in composites, Mech. Syst. Signal Process. 163 (June 2021) (2022) 108142, http://dx.doi.org/10.1016/j.ymssp.2021.108142, URL https://linkinghub.elsevier.com/retrieve/pii/S0888327021005227.

[33] J. Spytek, L. Ambrozinski, L. Pieczonka, Evaluation of disbonds in adhesively bonded multilayer plates through local wavenumber estimation, J. Sound Vib. 520 (April 2021) (2022) 116624, http://dx.doi.org/10.1016/j.jsv.2021.116624, URL https://linkinghub.elsevier.com/retrieve/pii/S0022460X21006350.

[34] J. Rose, Ultrasonic Waves in Solid Media, Cambridge University Press, Cambridge, 1999, p. 454, Ch..

[35] L.M. Brekhovskikh, Waves in Layered Media, Academic Press, 2012.

[36] D.A. Kiefer, GEWtool, 2023, http://dx.doi.org/10.5281/zenodo.10114244, URL https://github.com/dakiefer/GEWtool.

[37] D. Kiefer, Elastodynamic Quasi-Guided Waves for Transit-Time Ultrasonic Flow Metering (Ph.D. thesis), FAU University Press, 2022, http://dx.doi.org/10.25593/978-3-96147-550-6.

[38] H. Gravenkamp, A.A. Saputra, S. Duczek, High-order shape functions in the scaled boundary finite element method revisited, Arch. Comput. Methods Eng. 28 (2) (2021) 473–494, http://dx.doi.org/10.1007/s11831-019-09385-1.

[39] H. Gravenkamp, B. Plestenjak, D.A. Kiefer, Notes on osculations and mode tracing in semi-analytical waveguide modeling, Ultrasonics 135 (2023) 107112, http://dx.doi.org/10.1016/j.ultras.2023.107112.

[40] D. Chimenti, S. Rokhlin, P. Nagy, Physical Ultrasonics of Composites, Oxford University Press, 2011, http://dx.doi.org/10.1093/oso/9780195079609.001.0001, URL https://academic.oup.com/book/42000.

[41] D.A. Kiefer, M. Fink, S.J. Rupitsch, Simultaneous ultrasonic measurement of thickness and speed of sound in elastic plates using coded excitation signals, IEEE Trans. Ultrason. Ferroelectr. Freq. Control 64 (11) (2017) 1744–1757, http://dx.doi.org/10.1109/TUFFC.2017.2746900, URL http://ieeexplore.ieee.org/document/8022930/.

[42] T.E. Michaels, J.E. Michaels, M. Ruzzene, Frequency–wavenumber domain analysis of guided wavefields, Ultrasonics 51 (2011) 452–466, http://dx.doi.org/10.1016/j.ultras.2010.11.011, URL https://linkinghub.elsevier.com/retrieve/pii/S0041624X10001812.

[43] K.J. Schubert, A.S. Herrmann, On attenuation and measurement of Lamb waves in viscoelastic composites, Compos. Struct. 94 (1) (2011) 177–185, http://dx.doi.org/10.1016/j.compstruct.2011.07.003, URL https://linkinghub.elsevier.com/retrieve/pii/S0263822311002583.

[44] Z. Dworakowski, L. Ambrozinski, P. Packo, K. Dragan, T. Stepinski, Application of artificial neural networks for compounding multiple damage indices in lamb-wave-based damage detection, Struct. Control Health Monit. 22 (1) (2015) 50–61, http://dx.doi.org/10.1002/stc.1659, arXiv:https://onlinelibrary.wiley.com/doi/pdf/10.1002/stc.1659, URL https://onlinelibrary.wiley.com/doi/abs/10.1002/stc.1659.